Deciphering Nanoparticle Trafficking into Glioblastomas Uncovers an Augmented Antitumor Effect of Metronomic Chemotherapy

Melgious Jin Yan Ang, Jeehyun Yoon, Mingzhu Zhou, Han-Lin Wei, Yi Yiing Goh, Zhenglin Li, Jia Feng, Haifang Wang, Qianqian Su,* Derrick Sek Tong Ong,* and Xiaogang Liu*

Nanoparticles have been explored in glioblastomas as they can traverse the blood–brain barrier and target glioblastoma selectively. However, direct observation of nanoparticle trafficking into glioblastoma cells and their underlying intracellular fate after systemic administration remains uncharacterized. Here, based on high-resolution transmission electron microscopy experiments of an intracranial glioblastoma model, it is shown that ligand-modified nanoparticles can traverse the blood–brain barrier, endocytose into the lysosomes of glioblastoma cells, and undergo endolysosomal escape upon photochemical ionization. Moreover, an optimal dose of metronomic chemotherapy using dual-drug-loaded nanocarriers can induce an augmented antitumor effect directly on tumors, which has not been recognized in previous studies. Metronomic chemotherapy enhances antitumor effects 3.5-fold compared with the standard chemotherapy regimen using the same accumulative dose in vivo. This study provides a conceptual framework that can be used to develop metronomic nanoparticle regimens as a safe and viable therapeutic strategy for treating glioblastomas and other advanced-stage solid tumors.

1. Introduction

Glioblastoma (GBM), characterized by extensive microvascular proliferation and is considered the most infiltrative and aggressive form of solid brain tumors with poor prognoses.[1] The primary route of therapeutic delivery to GBM is intravenous, owing to its minimal invasiveness, ease of dose management, and competent delivery to multiple tumor regions.[2] However, the blood–brain barrier (BBB) severely restricts the non-selective entry of solutes from the blood into the brain parenchyma. In addition, several studies have concluded that an intact BBB in both orthotopic GBM xenografts and patients limits efficacious drug levels in the tumor.[3] Nanoparticles have recently attracted significant attention because they can traverse BBB, thereby enhancing the intratumoral chemotherapeutics and

M. J. Y. Ang, Y. Y. Goh, Z. Li, X. Liu
Department of Chemistry
National University of Singapore
Singapore 117543, Singapore
E-mail: chmlx@nus.edu.sg

M. J. Y. Ang, Y. Y. Goh, X. Liu
NUS Graduate School (ISEP)
National University of Singapore
Singapore 119077, Singapore

M. J. Y. Ang, Y. Y. Goh, X. Liu
The N1 Institute for Health
National University of Singapore
Singapore 117456, Singapore

J. Yoon, J. Feng, D. S. T. Ong
Department of Physiology
National University of Singapore
Singapore 117593, Singapore
E-mail: phsostd@nus.edu.sg

J. Yoon, D. S. T. Ong
NUS Center for Cancer Research
Yong Loo Lin School of Medicine
National University of Singapore
Singapore 117597, Singapore

M. Zhou, H.-L. Wei, H. Wang, Q. Su
Institute of Nanochemistry and Nanobiology
Shanghai University
Shanghai 200444, China
E-mail: chmsqq@shu.edu.cn

D. S. T. Ong
Institute of Molecular and Cell Biology (IMCB)
Agency for Science, Technology, and Research (A*STAR)
Singapore 138632, Singapore

D. S. T. Ong
National Neuroscience Institute
Singapore 308433, Singapore

targeting GBM selectively. These attributes confer tremendous potential to nanoparticles as multifunctional moieties that are capable of unraveling intricate GBM mechanisms and therapeutic responses.

Despite extensive prior research, there has been no direct experimental characterization of nanoparticles that elucidate the nanoparticle trafficking into GBM cells and their intracellular fate after intravenous administration.[2,4] Although conventional imaging modalities have been used in intravital microscopy or in ex vivo studies on extracted brain sections, these imaging modalities use indirect evidence to validate nanoparticles homing to brain tumors (Table S1, Supporting Information). However, this indirect evidence leads to a limited resolution range. Moreover, nanoparticle entry into brain tumors is highly challenging and requires overcoming multiple physiological barriers. Of note, nanoparticles have recently been shown to enter GBM predominantly through an active transendothelial process via brain endothelial cells.[3b] This major finding, together with other impeding factors, such as elevated interstitial tumor pressures and dense extracellular matrices in the tumor microenvironment, have alluded that nanoparticles may predominantly be localized in the perivascular niche within the tumor interstitium instead of being endocytosed into GBM cells.[4f,5] Resolving the controversy of the underlying fate of systemically administered brain targeting nanoparticles is crucial to improve therapeutic approaches for clinical translation of nanomedicine for GBM.

Herein, we report the direct characterization using transmission electron microscopy that validates the traversing nature of drug-encapsulated ligand-coated nanoparticles via BBB. Following intravenous administration in an orthotopic GBM xenograft model, these nanoparticles are endocytosed and transported to GBM cell lysosomes, followed by endolysosomal escape upon photochemical ionization into the cytosol (**Figure 1**a). We further probed the antitumor mechanisms of an optimized low-dose metronomic nanoparticle (MetNano) regimen. These mechanistic investigations provided substantial evidence that supports an augmented antitumor effect of metronomically administered nanoparticles directly on GBM cells, which was not found in previous studies (Figure 1b, Table S2, Supporting Information). Notably, the optimized MetNano regimen yielded an overall 3.5-fold improvement antitumor effects to the maximum tolerated dose in vivo, examined at the same accumulative drug dose. Our results justify an alternative therapeutic strategy for using MetNano regimens to improve the outcomes of glioblastomas and other advanced-stage solid tumors.

2. Results and Discussion

2.1. Preparation of Surface-Modified Multifunctional GBM Nanoparticles

We chose neodymium (Nd)-doped nanoparticles (NPs) in this study because of their superior photophysical properties such as uniformity and high biocompatibility, as seen in our previous biological studies.[6] We designed and synthesized core–multishell Nd-NPs with a previously established co-precipitation method to enhance their overall luminescence (Figure S1, Supporting Information).[7] Transmission electron microscopy (TEM) and powder X-ray diffraction (XRD) showed that the core $NaYF_4$:Yb/Er (20/2 mol%) denoted as Er-NPs had a uniform size of ≈25 nm and possessed a β-phase structure (Figure S2, Supporting Information). Upon excitation at 980 nm, Er-NPs yielded the expected upconversion peaks. Next, we fabricated an $NaYF_4$:Yb/Nd (10/40 mol%) epitaxial shell onto Er-NPs to form $NaYF_4$:Yb/Er (20/2 mol%)@$NaYF_4$:Yb/Nd (10/40 mol%) (denoted as Er@Nd-NPs). Moreover, we passivated another $NaYF_4$ optically inert epitaxial shell to form $NaYF_4$:Yb/Er(20/2 mol%)@$NaYF_4$:Yb/Nd(10/40 mol%)@$NaYF_4$ (denoted as Er@Nd@Y-NPs). TEM and XRD showed that both Er@Nd- and Er@Nd@Y-NPs had uniform diameters of ≈30 and 34 nm, respectively with β-phase structures (Figures S3 and S4, Supporting Information). We confirmed the existence of core–multishell Nd-NPs using high-angle annular dark-field imaging due to the contrast difference in high-angle scattered electrons between Nd^{3+} and Y^{3+} ions. Moreover, energy-dispersive X-ray spectroscopy analysis ascertained the key dopants in Er@Nd@Y-NPs (Figure 2a). We next examined the photoluminescence of Er@Nd- and Er@Nd@Y-NPs. The intensity enhancements of ≈4.7 and 3.6 fold were, respectively, observed for the upconverting peaks (542, 655 nm) and downshifting (980, 1060 nm) emission peaks after surface passivation (Figure S5, Supporting Information). The dominant energy transfer and key emissive peaks after 808 nm excitation are illustrated in an energy-level diagram (Figure S6, Supporting Information).[8]

Surface modifications of Er@Nd@Y-NPs were performed to render good biocompatibility, high drug loading capacity, and effective NP trafficking to GBM cells in vitro and in vivo. We selected human serum albumin proteins, poly(acrylic acid), and poly(ethylene glycol) biopolymers because they are known to confer superior physicochemical properties.[9] We designed a synthetic route and performed various surface modifications (Figure S7, Supporting Information). Fourier transform infrared (FTIR) spectroscopy confirmed the successful surface modifications from Er@Nd@Y-NPs to poly(acrylic acid)-coated@Er@Nd@Y (PAA-NPs) (Figure S8, Supporting Information). In addition, high-resolution TEM verified that PAA-NPs, human serum albumin and poly(acrylic acid)-coated@Er@Nd@Y (HSA-NPs), and BBB-crossing ANG2 peptide-coated TL-NPs were uniform in size with diameters, ≈38, 42, and 42 nm, respectively (**Figure 2**b and Figure S9, Supporting Information). Furthermore, we used dynamic light scattering measurements and verified the increase in hydrodynamic diameters of surface-modified NPs (Figure 2c, Table S3, Supporting Information). Notably, TL-NPs exhibited good colloidal stability in biologically relevant media, suggesting that the hard human serum albumin proteins, covalently coated onto PAA-NPs, bestow NPs with stealth properties during systemic circulation and block the undesirable, unbridled buildup of host serum proteins as seen previously (Figure S10, Supporting Information).[10] Finally, the NP zeta potential was measured, and the results agreed with published values (Figure S11, Supporting Information).[11] Quantitative photoluminescence measurements detected 68 human serum albumin proteins and 51 ANG2 peptides on each HSA- and TL-NP, respectively (Figure S12, Supporting Information).
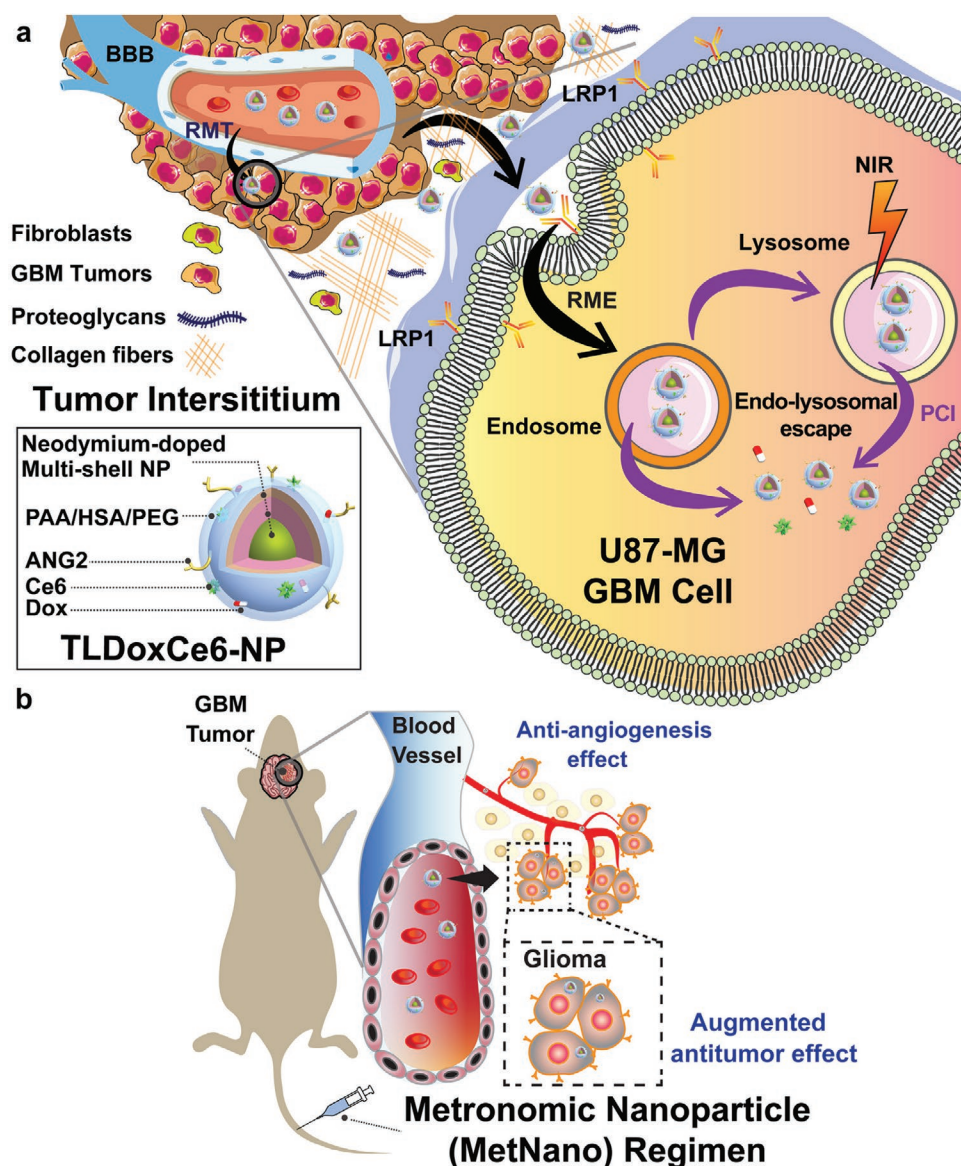
Figure 1. Nanoparticle trafficking into U87-MG glioma cells and a metronomic nanoparticle (NP) regimen possessing anti-angiogenesis and directed, augmented antitumor effects. a) Design of TLDoxCe6-NPs and the NP intraveous trafficking route. TLDoxCe6-NPs were made of neodymium-based NPs, which were surface-modified with a layer of poly(acrylic acid) and human serum albumin proteins, covalently tethered poly(ethylene glycol), and conjugated with BBB and U87-MG-glioma-targeting ANG2 peptides. TLDoxCe6-NPs selectivity target overexpressed LRP1 receptors on BBB and glioma tumors via receptor-mediated transcytosis (RMT) across BBB and receptor-mediated endocytosis (RME) into U87-MG glioma cells. Continuous-wave 808 nm excitation results in photochemical ionization that generates reactive oxygen species (ROS) intracellularly destabilizes and destroys the cell membrane, and renders the escape of TLDoxCe6-NPs. b) Schematic of the antitumor effects observed in the metronomic nanoparticle (MetNano) regimen, caused by the anti-angiogenesis effects on tumor endothelial cells and an augmented antitumor effect on glioma.

We loaded doxorubicin (Dox) and chlorin e6 (Ce6) to render the functionalities of synergistic chemo-photodynamic therapy. These drugs were selected because of their well-demonstrated clinical efficacy and potent antitumor effects.[12] The loading content and efficiency of Dox and Ce6 on our NPs were assessed with a maximum of ≈9% and 82% w/w, respectively (Table S4, Supporting Information). Drug release profiles were assessed at physiological and GBM tumor microenvironments.[13] Notably, drugs were rapidly released at pH 5.0 but not at pH 7.4 (Figure S13, Supporting Information). The drug loading onto TL-NPs showed

no premature drug leakage following high-speed centrifugation (Figure S14, Supporting Information). We subsequently measured luminescence decay at 650 nm and validated resonance energy transfer to Ce6 in TLCe6- and TLDoxCe6-NPs because their fluorescence decay lifetimes were decreased. The energy transfer efficiencies of TLCe6- and TLDoxCe6-NPs were calculated as 52% and 40%, respectively (Figure S15, Supporting Information). We examined the $^1O_2$ production using ABDA probes and confirmed its generation in Ce6- and TLDoxCe6-NPs (Figure S16, Supporting Information).
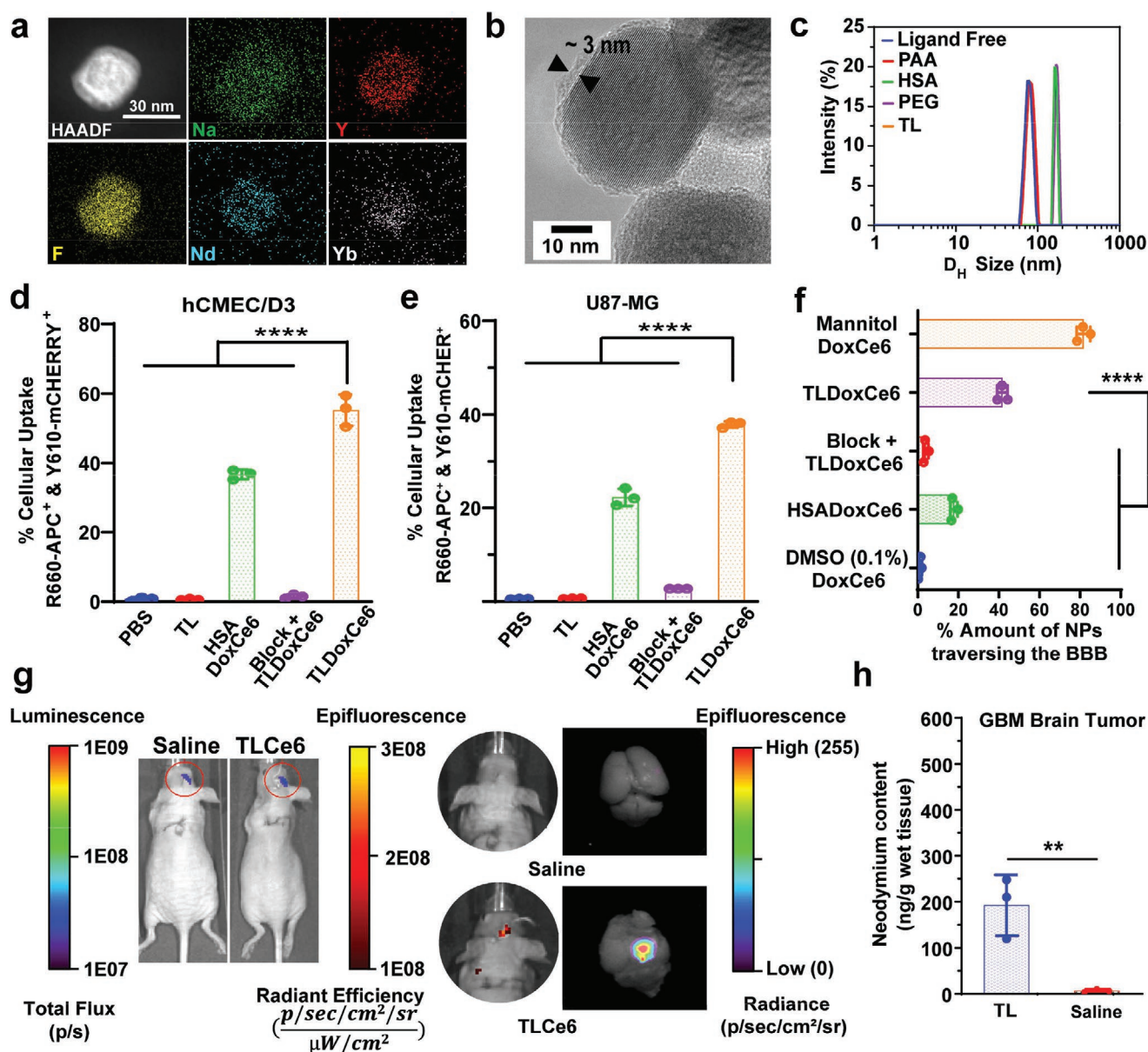
Figure 2. Nanoparticle (NP) characterizations and in vitro and in vivo bioimaging studies supporting the fact that NPs traverse BBB and localize within the GBM tumors. a) High-angle annular dark-field imaging and elemental mapping of a single Er@Nd@Y-NP, indicating contrast differences between Nd and Y lanthanide dopants and the spatial distribution of Na, Y, F, Nd, and Yb elements in the Nd^{3+}-based multishell nanostructure. Scale bar: 30 nm. b) High-resolution transmission electron microscopy (TEM) imaging of an as-synthesized TL-NP showing a diameter of ≈42 nm. c) Dynamic light scattering size distribution profiles of various surface-modified NPs. d,e) Bar graphs from flow cytometry analysis showed the percent cellular uptake of NPs into hCMEC/D3 and U87-MG cells, respectively. Percent cellular uptake is denoted by both R660-APC+ (Ce6) and Y610-mCHERRY+ (Dox) channels. Data represent means ± standard deviation (SD) ($n = 3$, biologically independent samples). The asterisk indicates that differences between the control groups are statistically significant based on an anaylsis of variance (ANOVA) test (****: $p < 0.001$, 1 = PBS, 2 = TL, 3 = HSADoxCe6-NPs, 4 = block+TLDoxCe6-NPs, and 5 = TLDoxCe6-NPs). All drug concentrations were normalized to 0.05 mg mL^{-1} of TLDoxCe6-NPs. f) Bar diagram indicating the relative amount of various NP control groups permeating across the in vitro BBB model, traversing across and entering the basolateral brain compartment, as determined from Dox fluorescence using a Dox calibration plot. Data represent means ± SD ($n = 3$, biologically independent samples). The asterisk indicates that differences between the control groups are statistically significant based on an ANOVA test (****: $p < 0.001$). g) Representative in vivo and ex vivo fluorescence and bioluminescence imaging of saline and TLCe6-NPs in an intracranial GBM mouse model. Mice and GBM brain imaging experiments were performed on day 13 post-tumor implantation. In vivo fluorescence detected at 680 nm under excitation at 640 nm for 5 s. Ex vivo epifluorescence imaging was performed under continuous-wave 808 nm excitation (0.2 W cm^{-2}), and the downshifting 980 nm luminescence was detected using a 950 nm long-pass filter, 0.5 ms exposure. h) Representative ICP-MS biodistribution measurement of an in vivo orthotopic GBM mouse model following one-time intravenous injection of TL-NPs (20 mg kg^{-1}) and saline (pH 7.4), and the major organs were harvested after 12 h. Data represent means ± SD ($n = 3$, biologically independent samples). The asterisk indicates that differences between saline and TL-NPs in the brain tumor are statistically significant, based on a two-tailed unpaired t-test (**: $p < 0.01$).

**ADVANCED
SCIENCE NEWS**

www.advancedsciencenews.com

**ADVANCED
MATERIALS**

www.advmat.de

2.2. Bioimaging Studies Confirm GBM NPs Traversed the BBB into the Interstitial Tumor Space In Vivo

We examined whether our GBM NPs could be endocytosed into GBM cells in vitro. Several studies have shown that the expression of low-density lipoprotein receptor-related protein 1 receptors (LRP1) is vital for NP trafficking across BBB through receptor-mediated transcytosis (RMT) and receptor-mediated endocytosis (RME) through several key internalization pathways into GBM cells by binding to ANG2 peptides (TFFYGGSRG-KRNNFKTEEY).[14] In agreement with previous results through direct immunofluorescence microscopy analysis, we verified the overexpression of LRP1 in human brain endothelial cells (hCMEC/D3) and human glioma (U87-MG) cells but not in HeLa cells (Figure S17, Supporting Information).[15] In addition, flow cytometry analysis showed the enhanced cellular uptake of TLDoxCe6-NPs into hCMEC/D3 and U87-MG cells, in part mediated by LRP1, because this uptake was reduced in the presence of free competing ANG2 peptides in the culture medium (Figure 2d,e and Figure S18, Supporting Information). Furthermore, both TL- and TLCe6-NPs did not affect the cell viability of hCMEC/D3 and U87-MG cells up to 400 µg mL^{-1} after 48 h incubation, suggesting their good in vitro biocompatibility (Figures S19 and S20, Supporting Information). We next evaluated the permeability effect of GBM NPs using an in vitro BBB model wherein the transendothelial electrical resistance (TEER) values provided a readout of the integrity of tight junctions at the BBB (Figure S21, Supporting Information). The measured optimal TEER values (>200 Ω cm^{-2}) indicate no compromise in BBB integrity in vitro, which is in agreement with published data for BBB transcytosis study.[16] Importantly, Dox fluorometric analyses suggested that TLDoxCe6-NPs traversed BBB more efficiently (>2-fold) than other control groups after 14 h incubation (Figure 2f). We further examined the ability of our NPs to target the GBM microenvironment in vivo. We used a well-established method to transplant firefly luciferase-labeled U87-MG GBM cells into athymic nude mouse brains that enabled us to monitor GBM growth noninvasively via bioluminescence signals.[11] On day 13 following tumor transplantation, we administered saline or TLCe6-NPs to the mice via a tail-vein injection and detected a strong emissive fluorescence from TLCe6-NPs at the 8 h time-point, but only negligible signals from the saline group (Figure 2g). Notably, there was colocalization of Ce6 fluorescence from TLCe6-NPs and the tumor bioluminescence, suggesting that TLCe6-NPs successfully localized within GBM tumors. To precisely demonstrate that TLCe6 fluorescence emanated from within brain tumors, we carefully extracted the brains of the same tumor-bearing mice and performed ex vivo epifluorescence near-infrared bioimaging. The brains of TLCe6-NPs treated mice gave strong 980 nm downshifting luminescence signals under 808 nm excitation, whereas minimal signals were detected in the saline group. Moreover, the designed nanotheranostic GBM NPs can provide valuable data on the precise location after intravenous administration. We also examined the biodistribution of TL-NPs in comparison with saline using inductively coupled plasma mass spectrometry (ICP-MS) analysis. Of note, we detected a relatively high Nd content from our NPs in the liver, and an elevated amount in the brain tumors of the tumor-bearing mice,

suggesting a good target selectivity of our TL-NPs in the GBM tumors (Figure 2h and Figure S22, Supporting Information). The high accumulation of TL-NPs within the liver is similar to that reported in other studies because of the large amount of NPs being sequestered by Kupffer cells.[17] Collectively, these bioimaging results provided macroscopic evidence to support the successful trafficking of NPs to traverse BBB and localize into the regions surrounding the implanted GBM tumors.

2.3. NP Trafficking into GBM and Endolysosomal Escape by Photochemical Ionization In Vivo

We examined the intravenously administered NPs using high-resolution TEM to determine whether transplanted GBM cells in an intracranial mouse model could endocytose NPs in vivo and study their underlying intracellular trafficking fate. Typically, in LRP1-mediated RME, clathrin predominantly mediates the cellular uptake of specific cargos, include proteins, NPs, metabolites, and viruses, by the invagination of the plasma membrane, a process known as the clathrin-mediated endocytosis (CME) pathway.[14c,18] In addition, there is strong evidence to suggest that major endocytosis pathways would lead to the formation of nanoparticle-containing early endosomes that are eventually sorted and matured into lysosomes.[14c] Therefore, we first examined the in vitro intracellular fate of TLDoxCe6-NPs undergoing LRP1-mediated RME in U87-MG cells (**Figure 3**a). Using a high magnification colocalization fluorescence experiment, we demonstrated that TLDoxCe6-NPs were found predominantly in the late endosomes and lysosomes after incubation for 8 h (Figure S23, Supporting Information). Of note, there was also an observable binding of free Dox to topoisomerase II protein in the nucleus.

To further study in vivo NP trafficking into GBM cells upon intravenous administration, we analyzed the extracted tumor-bearing brain sections by TEM that enabled us to probe the ultrastructure level with a resolution of 2 nm.[3b] We then scanned for cellular regions with glioma-like characteristics that comprise unusual organelle or cellular morphologies. Of note, we found regions with an abnormally large nucleolus, with irregularities and invaginations of the nuclear envelope (Figure S24, Supporting Information).[19] Other crucial evidence included the presence of numerous lipid droplets, which accumulated near the mitochondria, and the abnormal swollen mitochondrial morphology, with irregular and haphazard cristae arrangements. These findings concurred with published ultrastructure images that support the notion that NP localization is in glioma regions.[20] We scrutinized these glioma-like areas for NPs. Of note, our NPs were found within these glioma-like cellular regions, entrapped in either endosomes or lysosomes (Figure 3b–d). The observed endosomes appeared single membrane-bound spherical- or tubular-shaped, which is in agreement with reported ultrastructure images.[21] We also concurred with the identified morphologies of lysosomes, which have a single membrane and spherical morphology with regions of circular electron-rich dark patterns.[21] TEM imaging of other regions also showed that NPs were distributed in clusters within GBM endosomes and lysosomes. These results agree with published data that NP clusters can form
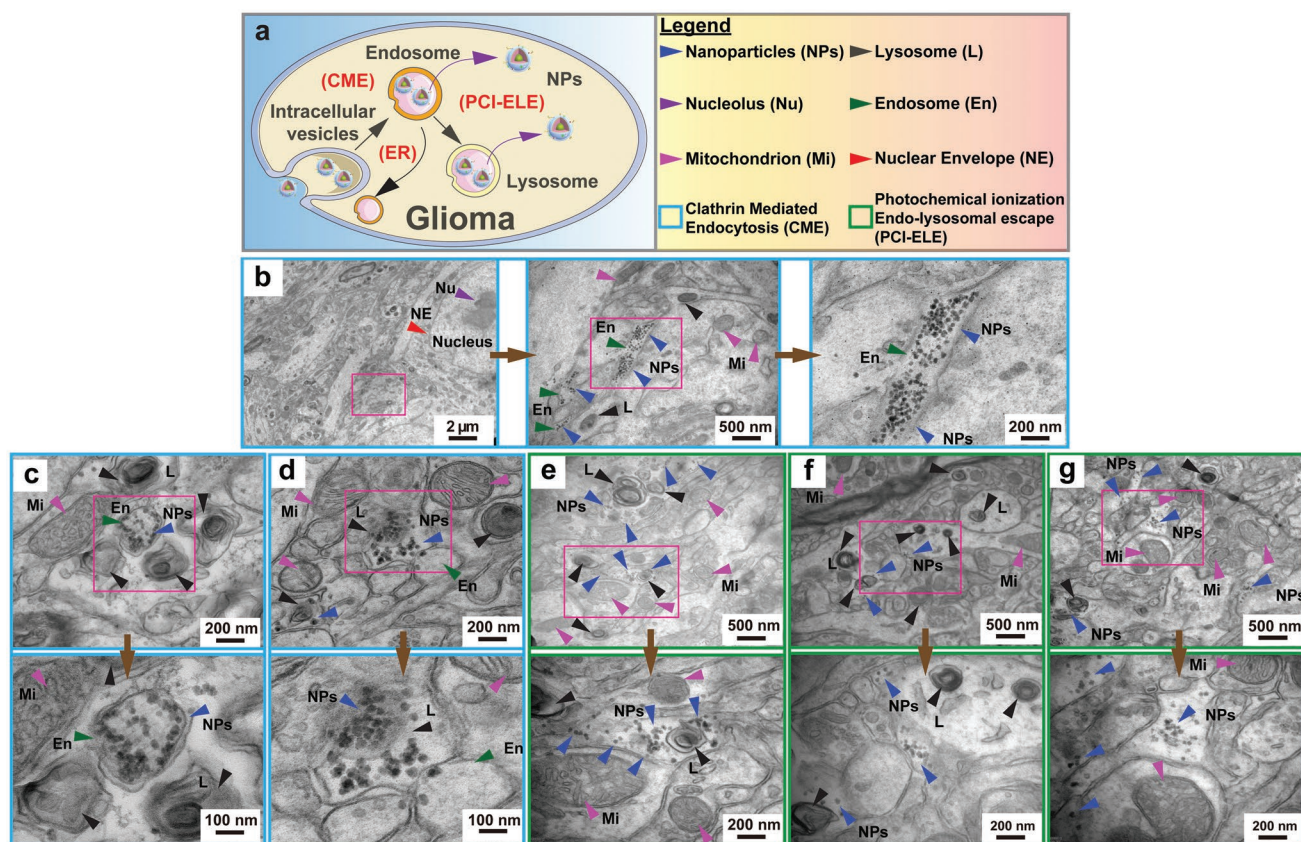
Figure 3. Direct observation using the transmission electron microscopy (TEM) investigations of GBM brain sections treated with nanoparticles (NPs). a) Schematic indicating various underlying fates of intravenously administered NPs: Clathrin-mediated endocytosis (CME), photochemical ionization endo-lysosomal escape (PCI-ELE), and endocytic recycling (ER). b) TEM ultrastructure analysis supporting that NPs undergo endosome maturation within U87-MG glioma cells and form clusters. c,d) Various glioma regions of different GBM brain sections showing the internalization and sorting of NPs into endosomes (En) before maturing into lysosomes (L). e–g) TEM ultrastructure analysis of regions where NPs have undergone photochemical ionization and induced endolysosomal escape (PCI-ELE). Magnified images are shown (pink box). The estimated average diameter of NPs in these images matched the diameters of the as-synthesized GBM NPs of ≈42 nm (n = 300 NPs). This was taken from at least 6 different brain tumor regions from various extracted brain-tissue samples.

after permeation in the cell membrane.[22] In addition, the NP localization in endosomes and lysosomes reflects endocytosis at different durations, given that NPs in endosomes would eventually be fused with lysosomes.[14c,23]

We next investigated the possibility of NPs to undertake endolysosomal escape via photochemical ionization (PCI). This process involved the induction of oxidative damage to the endolysosomal cell membranes by reactive oxygen species (ROS) to destabilize the membrane and cause leakage. We first confirmed the generation of singlet oxygen $^1O_2$ ROS using a U87-MG cell in vitro experiment and found that significant intracellular $^1O_2$ was generated in TLDoxCe6-NPs + 808 nm excitation as observed from the green luminescence but not in other control groups (Figure S25, Supporting Information). To induce intracellular $^1O_2$ in vivo, we irradiated the transplanted glioma region of the orthotopic GBM mice with a continuous-wave 808 nm laser at 1 W cm^{-2} for 20 min after 12 h post-tail-vein injection. Of note, TEM images showed that the systemic administered NPs were found either outside the endosomes or lysosomes, suggesting that they had undergone endolysosomal escape into the cytosol (Figure 3e–g). We also estimated that the

size of GBM NPs remained essentially unchanged (≈42 nm) on the basis of counting 300 NPs from at least 6 different regions, suggesting negligible degradation and good colloidal stability (Figure S26, Supporting Information).

2.4. Optimized MetNano Regimen Supports an Augmented Antitumor Effect on U87-MG In Vitro

We investigated implications from the direct observation of NPs that were endocytosed into U87-MG cells in vivo. Recently, several studies have administered drug-encapsulating NPs metronomically at 1/10 to 1/3 of the maximum tolerated dose (MTD) without prolonged drug-free breaks for various tumors, including glioblastoma (Table S2, Supporting Information). This paradigm shift is attractive because of its ability to control tumor growth without the need for substantial accumulation of NPs within tumors.[3a,5d] However, the antitumor mechanisms remain poorly understood. A majority of MetNano regimens suggest that NPs mainly target the endothelial cells of the tumor vasculature to exert an anti-angiogenesis effect, which
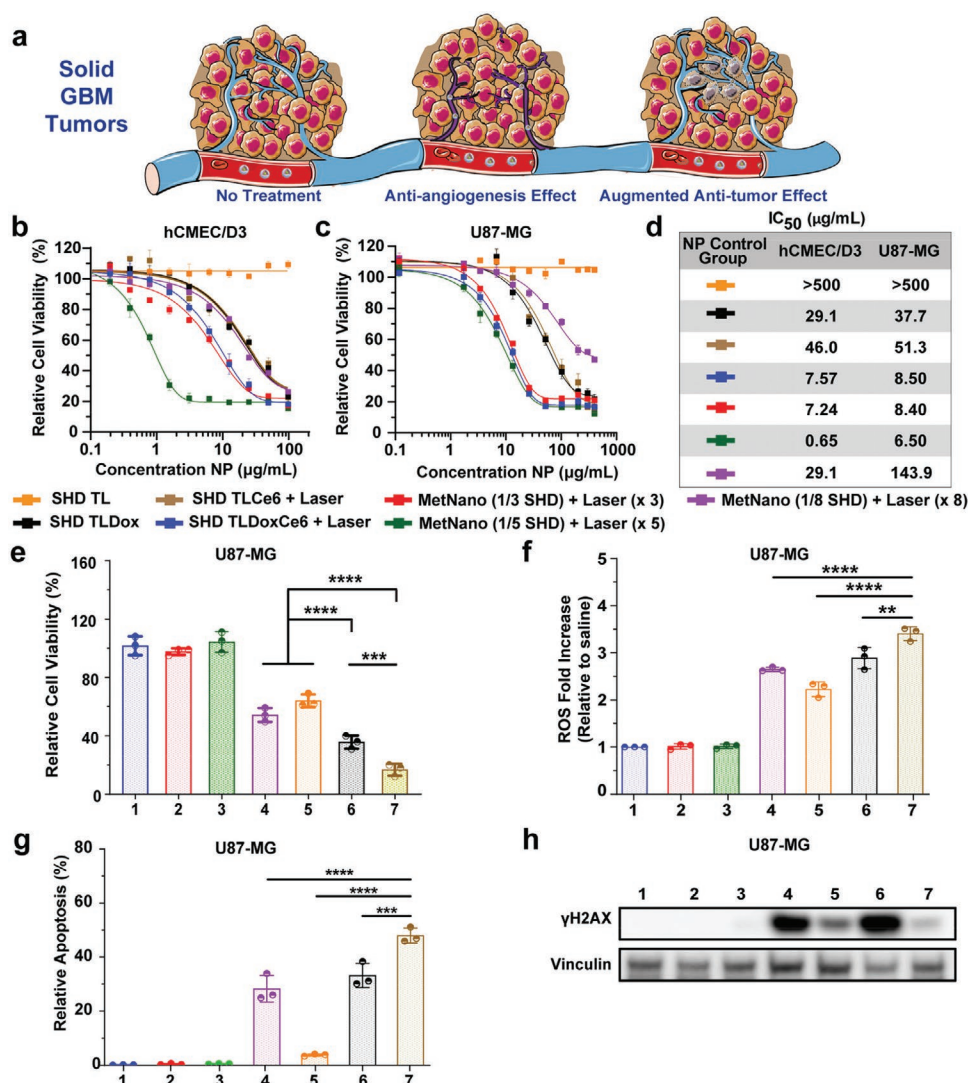
Figure 4. Optimized MetNano regimen supports augmented antitumor effect on glioma in vitro. a) A schematic diagram showing no treatment effects (left), anti-angiogenesis effect on tumor endothelial cells (middle), and augmented antitumor effect directly on glioma (right). b) Dose-response curves examining the anti-angiogenesis effect against the hCMEC/D3 cell line ranging from 0 to 100 μg mL^{-1}. c) Dose-response curves studying the anti-glioma effects against the U87-MG cell line ranging from 0 to 400 μg mL^{-1}. IC$_{50}$ values were calculated using Prism software by plotting log(inhibitor) versus response-variable slope (four parameters). Each concentration value within the control groups is represented as mean ± SD ($n = 3$, biologically independent samples, each concentration represented by 5 wells). d) Tabulated IC$_{50}$ values of various control groups in both hCMEC/D3 and U87-MG cell lines. e) Cell viabilities of U87-MG cells of various control groups incubated at the single high dose (SHD) fixed at 50 μg mL^{-1} of TLDoxCe6, and all treatment groups were normalized to ensure the same drug concentration for comparison (1 = saline, 2 = laser (x1), 3 = SHD TL, 4 = SHD TLDox, 5 = SHD TLCe6+laser, 6 = SHD TLDoxCe6+laser, 7 = MetNano TLDoxCe6 (1/5 SHD)+laser (x 5)). The error bars shown are means ± SD ($n = 3$, biologically independent samples). The asterisk indicates that differences between the control groups are statistically significant using an ANOVA test (***: $p < 0.001$, ****: $p < 0.001$). f) A bar diagram indicating the intracellular reactive oxygen species (ROS) fold increase for various control groups relative to the saline control group. The error bars shown are means ± SD ($n = 3$, biologically independent samples). The asterisk indicates that differences between the control groups are statistically significant using an ANOVA test (**: $p < 0.01$, ***: $p < 0.001$, ****: $p < 0.001$). g) Representative bar graph from flow cytometric analyses showing percent apoptotic cells in various control groups. Assessments were performed using cell populations that fell within the Annexin V$^+$ and PI$^+$ quadrant. Data represent means ± SD ($n = 3$, biologically independent samples). The asterisk indicates that differences between the control groups are statistically significant using an ANOVA test (***: $p < 0.001$, ****: $p < 0.001$). h) Western blot data on the γ-H2AX of various treatment control groups, with vinculin as the control.

presumably accounts for their antitumor effect. However, it is unclear whether drug-encapsulated NPs could directly exert an augmented antitumor effect on GBM cells.

We evaluated the cytotoxic effects of various MetNano regimens on hCMEC/D3 and U87-MG cells to assess the contribution of antitumor effects caused by anti-angiogenesis and direct antitumor effects on GBM in vitro (**Figure** 4a). We first optimized the crucial parameters to improve overall therapeutic efficacy against U87-MG cells. Notably, the 808 nm laser had a negligible heating effect on U87-MG cells,

ADVANCED
SCIENCE NEWS
www.advancedsciencenews.com

ADVANCED
MATERIALS
www.advmat.de

consistent with published data (Figure S27, Supporting Information).[24] We further determined the optimal photodynamic therapy (PDT) parameters of TLCe6-NPs with sufficient cytotoxicity. The single high dose (SHD), therapeutic laser exposure, and power density were 50 µg mL^{-1}, 20 min, and 1 W cm^{-2}, respectively. We next discovered a dose-dependent reduction in the cell viability of U87-MG with TLDox-NPs treatment with an optimal SHD at 50 µg mL^{-1}. We determined IC$_{50}$ values that involved various MetNano regimens due to data paucity. We studied the dose response on hCMEC/D3 in vitro to ascertain the anti-angiogenesis effect on brain endothelial cells using various MetNano regimens.[25] The cell viability of hCMEC/D3 was 12-fold lower comparing the one-fifth SHD MetNano regimen to the SHD TLDoxCe6+laser regimen (Figure 4b). We also quantified the apoptotic response of hCMEC/D3 with our treatment arms, which showed similar trends as our cell viability data when normalized at the same drug concentrations across various control groups (Figures S28 and S29, Supporting Information). Our findings were not surprising, given that others have shown that endothelial cells are sensitive to low-dose chemotherapeutics for prolonged duration.[26] Remarkably, we also found that the SHD TLDoxCe6+laser regimen was less efficacious than the one-fifth SHD MetNano regimen, suggesting that prolonged exposure to chemotherapeutics plays a critical role. Previous studies have also validated that drug exposure duration is a key parameter in causing cell death, which enables long-term tumor control with minimal host toxicity without the rapid onset of drug resistance.[26a,27]

We studied the dose response on U87-MG cells in vitro and found that the antiglioma efficacy of SHD regimens was not comparable to our findings in hCMEC/D3 cells. We attempted various MetNano regimens to determine the optimal dose and schedule. Notably, only the one-fifth SHD MetNano regimen resulted in a 1.3-fold greater cell viability reduction of U87-MG cells than with the SHD TLDoxCe6+laser regimen (Figure 4c,d). Although the antitumor effects were marginal, our in vivo ultrastructure data and in vitro U87-MG results provided strong evidence that supports an augmented antitumor effect directly on GBM cells by the endocytosed drug-encapsulated NPs, and this new insight was not addressed previously (Table S2, Supporting Information). We hypothesize that a metronomic administration involving a cocktail of encapsulated chemotherapeutic drugs within NPs that target the intrinsic cellular signaling pathways could further improve the antitumor effects against GBM cells, as exemplified in recent studies involving small molecular chemotherapuetics.[28] There were no observable effects with the one-third or one-eighth SHD MetNano regimens, which suggests that the effective therapeutic dose was not achieved. Thus, we focused on the one-fifth SHD MetNano regimen (hereafter referred to as the MetNano regimen) in subsequent experiments.

To confirm the antitumor effect from the MetNano regimen, we performed a cell viability comparison experiment and fixed the dose at 50 µg mL^{-1} of SHD TLDoxCe6+laser regimen along with the rest of the regimens, which had the same equivalent drug dose (Figure 4e). The dual treatment modality yielded a synergistic 2-fold improvement in efficacy over the single treatment modalities across various SHD regimens. Moreover, the

MetNano regimen had enhanced cytotoxicity compared with the SHD TLDoxCe6+laser regimen. Previous studies have indicated that both Dox- and chlorin E6-activated PDT can generate ROS to cause tumor cytotoxicity.[29] ROS measurements showed that the relative intracellular ROS levels within each treatment arm correlated with the trends of the cell viability and IC$_{50}$ experiments (Figure 4f). In particular, we found an intracellular ROS level of 1.2-fold higher in the MetNano regimen relative to the SHD TLDoxCe6+laser regimen. We then examined cell death populations in U87-MG cells and found similar patterns with an apoptosis level of 1.4-fold higher in the MetNano regimen than the SHD TLDoxCe6+laser regimen (Figure S30, Supporting Information). Both Dox- and chlorin-e6-activated PDT can also induce DNA double-stranded breaks, resulting in the phosphorylation of the H2AX histone (γH2AX).[30] We performed western blot analysis, and the results showed that the γH2AX levels were in agreement with the cell viability and IC$_{50}$ trends (Figure 4g).[31] Notably, γH2AX expression in the MetNano regimen was relatively lower than that in the SHD regimens, which involved TLDoxCe6+laser, TLCe6+laser, and TLDox regimens. We reasoned that this could be attributed to the relatively lower intracellular Dox and ROS exposure in the fractionated MetNano regimen than the SHD regimens, and chronically elevated ROS has been shown to cause H2AX protein degradation and the associated decrease of intracellular γH2AX proteins.[32]

2.5. Enhanced Therapeutic Efficacy of the MetNano Regimen in an Orthotopic GBM Xenograft Model

We first examined the MTD of GBM NPs in non-tumor-bearing nude mice based on published protocols.[33] The results showed that these GBM NPs were well-tolerated, even at a high dose of 100 mg kg^{-1} ($\approx 1.50 \times 10^{13}$ NPs), which falls within the typical dose range for tumor mouse model studies[17b] (Figure S31, Supporting Information). The body weight, sensory, and motor behavioral patterns of the mice were within an acceptable range relative to the saline control, suggesting the lack of acute toxicity effects. However, severe acute toxicity with a sudden weight loss was noted at the 150 mg kg^{-1} dose ($\approx 2.24 \times 10^{13}$ NPs) across all GBM NP control groups, indicating 100 mg kg^{-1} as MTD. We next evaluated the in vivo optimized dose to exert the therapeutic efficacy. We then tested the range from 5 to 20 mg kg^{-1} and showed that the optimized minimum dose was 20 mg kg^{-1} (Figure S32, Supporting Information). The 20 mg kg^{-1} dose inhibited GBM growth for at least 3 days, suggesting that a dosing schedule once every 3 days is feasible. We also examined the therapeutic efficacy in glioma-bearing mice, and they were divided into two groups: nondrug and drug (**Figure 5**a,b and Figure S33: Supporting Information). We chose the time period of 3 days in the MetNano regimen because several studies have shown the lengthy in vivo half-life duration of pegylated albumin NPs and sustained drug release that simulated the metronomic chemotherapy regimen without drug-free periods.[9b,c,34] As expected, the nondrug group yielded the highest bioluminescence 4 days post-treatment than the drug group. Comparing the average tumor increase in bioluminescence at the 4th day
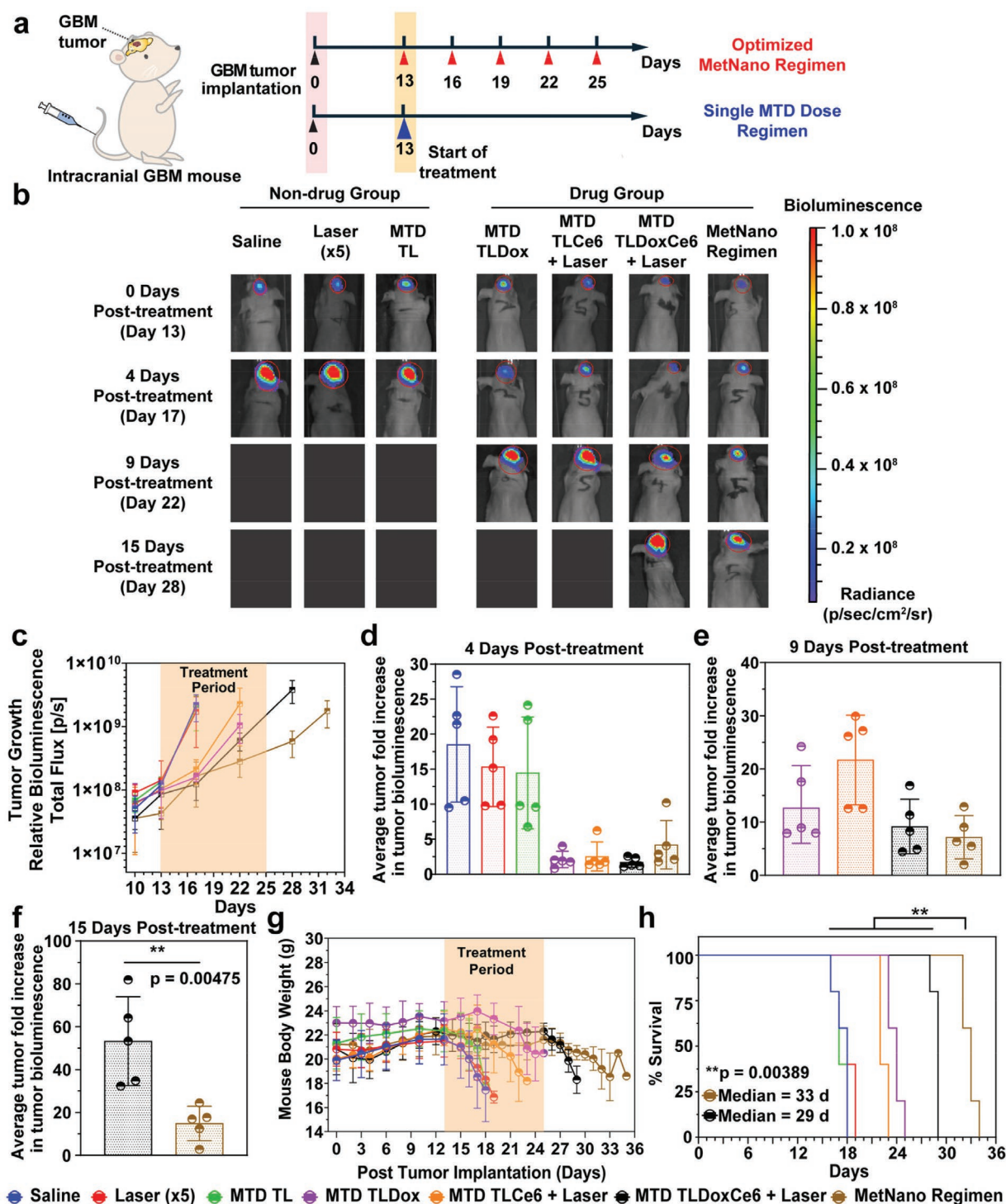
Figure 5. MetNano regimen shows enhanced efficacy compared with MTD regimen using an intracranial human GBM mouse model. a) Schematic of timeline comparing the treatment schedules of an optimized MetNano regimen with a single MTD regimen at the same cumulative dose (100 mg kg^{-1}). b) Representative luciferase bioluminescence images of various treatment arms. Non-drug group: saline, laser (x5), MTD TL, and drug group: MTD TLDox, MTD TLCe6 + laser, MTD TLDoxCe6 + laser, MetNano regimen: MetNano (1/5 MTD) + laser (x5), administered five times and every 3 days. MTD was fixed at TLDoxCe6 NPs, and all the treatment arms were normalized to ensure the same drug concentration for comparison. Images were taken on 0, 4, 9, and 15 days after the commencement of treatment on day 13. c) Relative tumor growth based on bioluminescence for all treatment arms. Relative tumor growth from bioluminescence signals using total flux (p/s). Data represent means ± SD ($n = 5$). d–f) Average tumor fold increase in tumor bioluminescence from baseline (day 13, the start of treatment): d) 4 days e) 9 days, and f) 15 days post-treatment. The error bars shown are means ± SD ($n = 5$). The asterisk indicates that differences in the MetNano and the MTD regimens are statistically significant, using a two-tailed unpaired t-test (**: $p < 0.01$). g) Bodyweight changes measurements for various treatment arms. h) Kaplan–Meier survival plots of various treatment arms. The experiment was performed using 5 mice per treatment arm and examined for statistical significance. A log-rank (Mantel–Cox) test was performed on the survival plots (**: $p < 0.01$).

post-treatment, the nondrug group was ≈15-fold higher, but the drug group was only ≈2.5-fold higher, indicative of reduced tumor growth (Figure 5c,d). Both MTD TLDoxCe6 + laser and MetNano regimens featured relatively strong antiglioma effects compared with monotherapies involving MTD TLDox and MTD TLCe6+laser, 9 days post-treatment (Figure 5e). Notably, the average tumor bioluminescence increase at 15 days post-treatment in the case of the MTD TLDoxCe6+laser regimen was ≈53-fold, but in the case of the MetNano regimen was only ≈15-fold, showing an almost 3.5-fold improvement in the overall efficacy (Figure 5f). We reasoned that the enhanced in vivo antitumor efficacy by the MetNano regimen could be due to the remodeling of the tumor microenvironment and normalization of the glioma vasculatures, which resulted in an enhanced nanoparticle delivery and distribution within tumors, which was shown in a previous study.[35] To validate this, we performed additional in vivo BBB penetration into glioma studies comparing MetNano and MTD regimens using the same net accumulative dose of 100 mg kg^{-1} and confirmed the improved delivery of our TLDoxCe6-NPs into glioma of MetNano regimen, which accounted for enhanced therapeutic efficacy (Figure S34, Supporting Information). However, glioma suppression was temporary, with tumor recurrence upon treatment termination. The glioma-bearing nude mice treated in the nondrug group also demonstrated significant body weight loss reflecting the intensifying brain damage and appetite loss as GBM progressed (Figure 5g). By contrast, marginal weight changes were found in the drug group, suggesting that the treatments were efficacious in inhibiting GBM growth without any acute toxicity. Survival analyses demonstrated improved survival in the MetNano regimen compared with the MTD TLDoxCe6+laser regimen (Figure 5h). Furthermore, the in vivo toxicity of the treatment arms was studied using histological tissue hematoxylin and eosin staining. In agreement with the measured body weights, neither pathological changes nor inflammatory infiltrate markers were observed even with various MTD treatment arms, suggesting a high in vivo biocompatibility (Figure S35, Supporting Information).

To further validate bioluminescence results, we performed immunofluorescence microscopy analysis of extracted brain sections in each of the drug group controls. At 9 days post-treatment, the mouse brains were sectioned and stained for the markers of apoptotic cell death (TUNEL), proliferation rate (Ki67) and microvessel density for endothelial cells (CD31). Tumors treated with the MetNano regimen showed the highest level of apoptosis relative to the other treatment arms (Figure S36, Supporting Information). Accordingly, cell proliferation was also the lowest in the mouse tumors that were subjected to the MetNano regimen, as revealed by Ki67 immunostaining (Figure S37, Supporting Information). We further examined CD31 and discovered a significant reduction of tumor endothelial cells in the MetNano regimen compared with other MTD regimens. This validated a potent anti-angiogenesis effect by the MetNano regimen (Figure S38, Supporting Information). Taken together, these results indicate the safe use as well as the enhanced in vivo therapeutic efficacy of the MetNano regimen compared with the MTD regimens in an orthotopic GBM xenograft mouse model.

3. Conclusions

This study presents direct evidence of systemically administered NPs that traverse BBB and were endocytosed into the lysosomes of transplanted glioblastoma cells in an orthotopic GBM xenograft mouse model, which was followed by lysosomal escape upon photochemical ionization. We showed strong evidence to support that the antitumor mechanisms of optimized MetNano regimens were caused by an anti-angiogenesis and augmented antitumor effects; the latter were not recognized in previous MetNano regimen studies. We further showed that the MetNano regimen elicited a 3.5-fold therapeutic response compared with the MTD regimen in vivo and suppressed tumor cell proliferation, increased apoptosis, and reduced tumor angiogenesis. Thus, our study provides strong evidence for the possible application of MetNano regimens to treat GBM and possibly other advanced-stage solid tumors.

4. Experimental Section

The experimental details are provided in the Supporting Information.

Supporting Information

Supporting Information is available from the Wiley Online Library or from the author.

Conflict of Interest

The authors declare no conflict of interest.

Author Contributions

A.J.Y.M. and X.L. conceived and initiated the project. X.L., D.S.T.O., Q.Q.S. supervised the project and led the collaboration efforts. A.J.Y.M, with support from Y.Y.G., carried out the surface-modified nanoparticle synthesis, in vitro therapeutic assessments of endothelial and glioma cell cultures, in vivo therapeutic administration, and health condition monitoring glioma-bearing mice, bioimaging, and TEM ultrastructural capture and analyses. J.Y.F.J. carried out the western blot analysis, brain section immunohistochemical staining, and analyses. J.Y. performed the glioma implantation in the animal work. Z.L. assisted in the multiple

**ADVANCED
SCIENCE NEWS**

www.advancedsciencenews.com

**ADVANCED
MATERIALS**

www.advmat.de

intravenous tail-vein injections of GBM nanoparticles. A.J.Y.M., M.Z., Y.L., Q.Q.S. were engaged in biodistribution animal studies and TEM processing on brain tumor sections and capturing the images. A.J.Y.M., Q.Q.S., H.W. assisted in analyzing the TEM ultrastructural images on the brain sections. A.J.Y.M. and X.L. wrote the manuscript with input from all authors.

[1] a) P. Y. Wen, S. Kesari, *N. Engl. J. Med.* **2008**, *359*, 492; b) S. Das, P. A. Marsden, *N. Engl. J. Med.* **2013**, *369*, 1561.

[2] J. V. Gregory, P. Kadiyala, R. Doherty, M. Cadena, S. Habeel, E. Ruoslahti, P. R. Lowenstein, M. G. Castro, J. Lahann, *Nat. Commun.* **2020**, *11*, 5687.

[3] a) C. D. Arvanitis, G. B. Ferraro, R. K. Jain, *Nat. Rev. Cancer* **2020**, *20*, 26; b) S. Sindhwani, A. M. Syed, J. Ngai, B. R. Kingston, L. Maiorino, J. Rothschild, P. MacMillan, Y. Zhang, N. U. Rajesh, T. Hoang, J. L. Y. Wu, S. Wilhelm, A. Zilman, S. Gadde, A. Sulaiman, B. Ouyang, Z. Lin, L. Wang, M. Egeblad, W. C. W. Chan, *Nat. Mater.* **2020**, *19*, 566; c) J. N. Sarkaria, L. S. Hu, I. F. Parney, D. H. Pafundi, D. H. Brinkmann, N. N. Laack, C. Giannini, T. C. Burns, S. H. Kizilbash, J. K. Laramy, K. R. Swanson, T. J. Kaufmann, P. D. Brown, N. Y. R. Agar, E. Galanis, J. C. Buckner, W. F. Elmquist, *Neuro-Oncology (Cary, NC, U. S.)* **2018**, *20*, 184.

[4] a) A. Galstyan, J. L. Markman, E. S. Shatalova, A. Chiechi, A. J. Korman, R. Patil, D. Klymyshyn, W. G. Tourtellotte, L. L. Israel, O. Braubach, V. A. Ljubimov, L. A. Mashouf, A. Ramesh, Z. B. Grodzinski, M. L. Penichet, K. L. Black, E. Holler, T. Sun, H. Ding, A. V. Ljubimov, J. Y. Ljubimova, *Nat. Commun.* **2019**, *10*, 3850; b) J. L. Huang, G. Jiang, Q. X. Song, X. Gu, M. Hu, X. L. Wang, H. H. Song, L. P. Chen, Y. Y. Lin, D. Jiang, J. Chen, J. F. Feng, Y. M. Qiu, J. Y. Jiang, X. G. Jiang, H. Z. Chen, X. L. Gao, *Nat. Commun.* **2017**, *8*, 15144; c) F. C. Lam, S. W. Morton, J. Wyckoff, T. L. Vu Han, M. K. Hwang, A. Maffa, E. Balkanska-Sinclair, M. B. Yaffe, S. R. Floyd, P. T. Hammond, *Nat. Commun.* **2018**, *9*, 1991; d) M. Wu, H. Zhang, C. Tie, C. Yan, Z. Deng, Q. Wan, X. Liu, F. Yan, H. Zheng, *Nat. Commun.* **2018**, *9*, 4777; e) M. F. Kircher, A. de la Zerda, J. V. Jokerst, C. L. Zavaleta, P. J. Kempen, E. Mittra, K. Pitter, R. Huang, C. Campos, F. Habte, R. Sinclair, C. W. Brennan, I. K. Mellinghoff, E. C. Holland, S. S. Gambhir, *Nat. Med.* **2012**, *18*, 829; f) J. Xue, Z. Zhao, L. Zhang, L. Xue, S. Shen, Y. Wen, Z. Wei, L. Wang, L. Kong, H. Sun, Q. Ping, R. Mo, C. Zhang, *Nat. Nanotechnol.* **2017**, *12*, 692.

[5] a) R. T. Tong, Y. Boucher, S. V. Kozin, F. Winkler, D. J. Hicklin, R. K. Jain, *Cancer Res.* **2004**, *64*, 3731; b) S. Wilhelm, A. J. Tavares, Q. Dai, S. Ohta, J. Audet, H. F. Dvorak, W. C. W. Chan, *Nat. Rev. Mater.* **2016**, *1*, 16014; c) Q. Dai, S. Wilhelm, D. Ding, A. M. Syed, S. Sindhwani, Y. Zhang, Y. Y. Chen, P. MacMillan, W. C. W. Chan, *ACS Nano* **2018**, *12*, 8423; d) R. K. Jain, T. Stylianopoulos, *Nat. Rev. Clin. Oncol.* **2010**, *7*, 653.

[6] a) M. Zhou, X. Ge, D. M. Ke, H. Tang, J. Z. Zhang, M. Calvaresi, B. Gao, L. Sun, Q. Su, H. Wang, *Front. Chem.* **2019**, *7*, 218; b) S. Chen, A. Z. Weitemier, X. Zeng, L. He, X. Wang, Y. Tao, A. J. Y. Huang, Y. Hashimotodani, M. Kano, H. Iwasaki, L. K. Parajuli, S. Okabe, D. B. L. Teh, A. H. All, I. Tsutsui-Kimura, K. F. Tanaka, X. Liu, T. J. McHugh, *Science* **2018**, *359*, 679; c) X. Zeng, S. Chen, A. Weitemier, S. Han, A. Blasiak, A. Prasad, K. Zheng, Z. Yi, B. Luo, I. H. Yang, N. Thakor, C. Chai, K. L. Lim, T. J. McHugh, A. H. All, X. Liu, *Angew. Chem., Int. Ed.* **2019**, *58*, 9262.

[7] a) F. Wang, R. Deng, X. Liu, *Nat. Protoc.* **2014**, *9*, 1634; b) S. Han, R. Deng, X. Xie, X. Liu, *Angew. Chem., Int. Ed.* **2014**, *53*, 11702.

[8] a) B. Zhou, J. Huang, L. Yan, X. Liu, N. Song, L. Tao, Q. Zhang, *Adv. Mater.* **2019**, *31*, 1806308; b) Y. Zhong, G. Tian, Z. Gu, Y. Yang, L. Gu, Y. Zhao, Y. Ma, J. Yao, *Adv. Mater.* **2014**, *26*, 2831.

[9] a) L. Xiong, T. Yang, Y. Yang, C. Xu, F. Li, *Biomaterials* **2010**, *31*, 7078; b) F. F. An, X. H. Zhang, *Theranostics* **2017**, *7*, 3667; c) J. S. Suk, Q. Xu, N. Kim, J. Hanes, L. M. Ensign, *Adv. Drug Delivery Rev.* **2016**, *99*, 28.

[10] T. Sabri, P. D. Pawelek, J. A. Capobianco, *ACS Appl. Mater. Interfaces* **2018**, *10*, 26947.

[11] D. Ni, J. Zhang, W. Bu, H. Xing, F. Han, Q. Xiao, Z. Yao, F. Chen, Q. He, J. Liu, S. Zhang, W. Fan, L. Zhou, W. Peng, J. Shi, *ACS Nano* **2014**, *8*, 1231.

[12] a) S. Voulgaris, M. Partheni, M. Karamouzis, P. Dimopoulos, N. Papadakis, H. P. Kalofonos, *Am. J. Clin. Oncol.* **2002**, *25*, 60; b) E. S. Villodre, F. C. Kipper, A. O. Silva, G. Lenz, P. Lopez, *Mol. Neurobiol.* **2018**, *55*, 4185.

[13] I. F. Tannock, D. Rotin, *Cancer Res.* **1989**, *49*, 4373.

[14] a) Y. Bertrand, J. C. Currie, J. Poirier, M. Demeule, A. Abulrob, D. Fatehi, D. Stanimirovic, H. Sartelet, J. P. Castaigne, R. Beliveau, *Br. J. Cancer* **2011**, *105*, 1697; b) B. Oller-Salvia, M. Sanchez-Navarro, E. Giralt, M. Teixido, *Chem. Soc. Rev.* **2016**, *45*, 4690; c) J. J. Rennick, A. P. R. Johnston, R. G. Parton, *Nat. Nanotechnol.* **2021**, *16*, 266.

[15] Proteinatlas.org, https://www.proteinatlas.org/ENSG00000123384-LRP1/cell (accessed: June 2021).

[16] B. P. Daniels, L. Cruz-Orengo, T. J. Pasieka, P. O. Couraud, I. A. Romero, B. Weksler, J. A. Cooper, T. L. Doering, R. S. Klein, *J. Neurosci. Methods* **2013**, *212*, 173.

[17] a) Y. N. Zhang, W. Poon, A. J. Tavares, I. D. McGilvray, W. C. W. Chan, *J. Controlled Release* **2016**, *240*, 332; b) B. Ouyang, W. Poon, Y. N. Zhang, Z. P. Lin, B. R. Kingston, A. J. Tavares, Y. Zhang, J. Chen, M. S. Valic, A. M. Syed, P. MacMillan, J. Couture-Senecal, G. Zheng, W. C. W. Chan, *Nat. Mater.* **2020**, *19*, 1362.

[18] a) C. Pucci, D. De Pasquale, A. Marino, C. Martinelli, S. Lauciello, G. Ciofani, *ACS Appl. Mater. Interfaces* **2020**, *12*, 29037; b) M. Sousa de Almeida, E. Susnik, B. Drasler, P. Taladriz-Blanco, A. Petri-Fink, B. Rothen-Rutishauser, *Chem. Soc. Rev.* **2021**, *50*, 5397.

[19] a) A. N. Malhas, D. J. Vaux, *Adv. Exp. Med. Biol.* **2014**, *773*, 523; b) J. C. Sipe, M. M. Herman, L. J. Rubinstein, *Am. J. Pathol.* **1973**, *73*, 589; c) L. Montanaro, D. Trere, M. Derenzini, *Am. J. Pathol.* **2008**, *173*, 301.

[20] G. Arismendi-Morillo, *Biochim. Biophys. Acta* **2011**, *1807*, 602.

[21] J. Huotari, A. Helenius, *EMBO J.* **2011**, *30*, 3481.

[22] M. Liu, Q. Li, L. Liang, J. Li, K. Wang, J. Li, M. Lv, N. Chen, H. Song, J. Lee, J. Shi, L. Wang, R. Lal, C. Fan, *Nat. Commun.* **2017**, *8*, 15646.

[23] a) J. P. Luzio, P. R. Pryor, N. A. Bright, *Nat. Rev. Mol. Cell Biol.* **2007**, *8*, 622; b) F. R. Maxfield, T. E. McGraw, *Nat. Rev. Mol. Cell Biol.* **2004**, *5*, 121.

[24] Y. F. Wang, G. Y. Liu, L. D. Sun, J. W. Xiao, J. C. Zhou, C. H. Yan, *ACS Nano* **2013**, *7*, 7200.

[25] a) J. Drevs, J. Fakler, S. Eisele, M. Medinger, G. Bing, N. Esser, D. Marme, D. Unger, *Anticancer Res.* **2004**, *24*, 1759; b) R. S. Kerbel, B. A. Kamen, *Nat. Rev. Cancer* **2004**, *4*, 423.

[26] a) G. Bocci, K. C. Nicolaou, R. S. Kerbel, *Cancer Res.* **2002**, *62*, 6938; b) E. Pasquier, M. P. Tuset, J. Street, S. Sinnappan, K. L. MacKenzie, D. Braguer, N. Andre, M. Kavallaris, *Angiogenesis* **2013**, *16*, 373.

**ADVANCED
SCIENCE NEWS**

www.advancedsciencenews.com

**ADVANCED
MATERIALS**

www.advmat.de

[27] a) S. D. Weitman, E. Glatstein, B. A. Kamen, *J. Clin. Oncol.* **1993**, *11*, 820; b) B. A. Kamen, E. Rubin, J. Aisner, E. Glatstein, *J. Clin. Oncol.* **2000**, *18*, 2935.

[28] a) J. M. Fernandes Neto, E. Nadal, E. Bosdriesz, S. N. Ooft, L. Farre, C. McLean, S. Klarenbeek, A. Jurgens, H. Hagen, L. Wang, E. Felip, A. Martinez-Marti, A. Vidal, E. Voest, L. F. A. Wessels, O. van Tellingen, A. Villanueva, R. Bernards, *Nat. Commun.* **2020**, *11*, 3157; b) M. Zoetemelk, G. M. Ramzy, M. Rausch, T. Koessler, J. R. van Beijnum, A. Weiss, V. Mieville, S. R. Piersma, R. R. de Haas, C. Delucinge-Vivier, A. Andres, C. Toso, A. A. Henneman, S. Ragusa, T. V. Petrova, M. Docquier, T. A. McKee, C. R. Jimenez, Y. Daali, A. W. Griffioen, L. Rubbia-Brandt, P. Y. Dietrich, P. Nowak-Sliwinska, *Mol. Oncol.* **2020**, *14*, 2894; c) A. E. Yesilkanal, D. Yang, A. Valdespino, P. Tiwari, A. U. Sabino, L. C. Nguyen, J. Lee, X. H. Xie, S. Sun, C. Dann, L. Robinson-Mailman, E. Steinberg, T. Stuhlmiller, C. Frankenberger, E. Goldsmith, G. L. Johnson, A. F. Ramos, M. R. Rosner, *eLife* **2021**, 10, 59696; d) R. S. Narayan, P. Molenaar, J. Teng, F. M. G. Cornelissen, I. Roelofs, R. Menezes, R. Dik, T. Lagerweij, Y. Broersma, N. Petersen, J. A. Marin Soto, E. Brands, P. van Kuiken, M. C. Lecca, K. J. Lenos, S. In't Veld, W. van Wieringen, F. F. Lang, E. Sulman, R. Verhaak, B. G. Baumert, L. J. A. Stalpers, L. Vermeulen, C. Watts, D. Bailey, B. J. Slotman, R. Versteeg, D. Noske, P. Sminia, B. A. Tannous, T. Wurdinger, J. Koster, B. A. Westerman, *Nat. Commun.* **2020**, *11*, 2935.

[29] a) K. C. Nitiss, J. L. Nitiss, *Clin. Cancer Res.* **2014**, *20*, 4737; b) N. M. Idris, M. K. Gnanasammandhan, J. Zhang, P. C. Ho, R. Mahendran, Y. Zhang, *Nat. Med.* **2012**, *18*, 1580.

[30] a) P. K. Singal, N. Iliskovic, *N. Engl. J. Med.* **1998**, *339*, 900; b) U. S. Srinivas, B. W. Q. Tan, B. A. Vellayappan, A. D. Jeyasekharan, *Redox Biol.* **2019**, *25*, 101084.

[31] a) M. A. Kang, E. Y. So, A. L. Simons, D. R. Spitz, T. Ouchi, *Cell Death Dis.* **2012**, *3*, 249; b) I. H. Goldberg, *Free Radical Biol. Med.* **1987**, *3*, 41.

[32] T. Gruosso, V. Mieulet, M. Cardon, B. Bourachot, Y. Kieffer, F. Devun, T. Dubois, M. Dutreix, A. Vincent-Salomon, K. M. Miller, F. Mechta-Grigoriou, *EMBO Mol. Med.* **2016**, *8*, 527.

[33] a) K. S. Chu, A. N. Schorzman, M. C. Finniss, C. J. Bowerman, L. Peng, J. C. Luft, A. J. Madden, A. Z. Wang, W. C. Zamboni, J. M. DeSimone, *Biomaterials* **2013**, *34*, 8424; b) R. Mohammadpour, D. L. Cheney, J. W. Grunberger, M. Yazdimamaghani, J. Jedrzkiewicz, K. J. Isaacson, M. A. Dobrovolskaia, H. Ghandehari, *J. Controlled Release* **2020**, *324*, 471.

[34] A. D. AlQahtani, D. O'Connor, A. Domling, S. K. Goda, *Biomed. Pharmacother.* **2019**, *113*, 108750.

[35] a) X. Luan, Y. Y. Guan, J. F. Lovell, M. Zhao, Q. Lu, Y. R. Liu, H. J. Liu, Y. G. Gao, X. Dong, S. C. Yang, L. Zheng, P. Sun, C. Fang, H. Z. Chen, *Biomaterials* **2016**, *95*, 60; b) R. K. Jain, *Science* **2005**, *307*, 58; c) Y. Chen, X. Liu, H. Yuan, Z. Yang, C. A. von Roemeling, Y. Qie, H. Zhao, Y. Wang, W. Jiang, B. Y. S. Kim, *Adv. Sci.* **2019**, *6*, 1802070.